

---



---

# TIMESCALE DYNAMICS OF COVID-19 PANDEMIC WAVES: THE CASE OF GREECE

---



---

✉ **Dimitris M. Manias**<sup>1,\*</sup>, ✉ **Dimitris G. Patsatzis**<sup>2</sup>, ✉ **Dimitris A. Goussis**<sup>3,4</sup>

<sup>(1)</sup> Department of Mathematics, *Khalifa University of Science and Technology*,  
Abu Dhabi 127788, United Arab Emirates

<sup>(2)</sup> Modelling Engineering Risk and Complexity, *Scuola Superiore Meridionale*, Naples 80138, Italy

<sup>(3)</sup> Department of Mechanical Engineering, *Khalifa University of Science and Technology*,  
Abu Dhabi 127788, United Arab Emirates

<sup>(4)</sup> Research and Innovation Center on CO<sub>2</sub> and H<sub>2</sub>, *Khalifa University of Science and Technology*,  
Abu Dhabi 127788, United Arab Emirates

December 13, 2023

## ABSTRACT

The results of an alternative methodology for making predictions about the COVID-19 pandemic in Greece are presented. Instead of focusing on the various population profiles (subjected to instabilities introduced by the fitting process), this methodology focuses on the time scale that characterises the intensity and duration of the *outbreak phase*. Therefore, instead of predicting the peak of active cases, here their inflection point is predicted (the point where the increase of active cases stops accelerating and starts decelerating). Since the inflection point precedes the peak, this methodology can serve as an early warning of the peak. In addition, the paths between the various populations (healthy, exposed, infected, etc) that contribute the most to the *outbreak phase* are identified.

---

**Keywords** Population dynamics · COVID-19 · Computational Singular Perturbation · time scale analysis

## 1 Introduction

The major effort in making predictions on the spread of COVID-19 focuses on the temporal evolution of various populations, notably active cases and deaths. Here, the employment of Computational Singular Perturbation (CSP) [1–3] is proposed as an alternative methodological approach for the analysis of COVID-19 pandemics compartmental models. The analysis is based on the time scale that characterises the *outbreak phase* (the period in which the number of active cases increases) and employs tools used for the multi-scale analysis of models in chemical kinetics, biology and pharmacokinetics. CSP is an algorithmic method of Geometrical Singular Perturbation Analysis (GSPA), which is employed in multi-scale dynamical systems; i.e., systems that are driven by processes evolving in a wide range of fast/slow time scales. In such systems, the processes characterized by the fast time scales become quickly exhausted and form low dimensional surfaces in the tangent space, well-known as Slow Invariant Manifolds (SIM) [4–6]. The trajectories of the system are then confined to evolve on the SIM, governed by the processes which are characterized by the remaining slow time scales. Recently, a physics-informed machine learning approach was introduced for the computation of SIMs, in the spirit of GSPA [7]. CSP offers a complete set of diagnostic tools for identifying the variables and physical processes related to (i) the fast time scales, which contribute to the formation of the SIM and (ii) the slow time scales that govern the dominant slow dynamics of the system. The CSP tools have been employed for gaining physical understanding of chemical kinetic mechanisms [8–18] and other multi-scale physical problems encountered in systems biology [19, 20] and population dynamics [21].

---

\*Corresponding Author: dimitris.manias@ku.ac.ae

The utilization of CSP offers significant advantages for analyzing epidemiological models, particularly in compartmental contexts. CSP's relevance stems from its compatibility with multi-scale epidemiological models, as demonstrated in various studies [22–26]. Unlike solution-based approaches, CSP focuses on system dynamics, avoiding issues like non-identifiability. It also provides a systems-level understanding, surpassing the capabilities of sensitivity analysis in distinguishing fast and slow dynamics. CSP's effectiveness in exploring dynamical systems with explosive eigenvalues, as seen in the initial exponential growth phase of COVID-19 [27–29]. The presence of a positive or explosive eigenvalue, which is a key characteristic during the exponential growth phase of COVID-19 pandemics, is a well-established concept [30, 31]. CSP methodology, known for its effectiveness in studying dynamical systems with such eigenvalues [21, 32–34], is therefore a logical choice for analyzing the rapid expansion of COVID-19.

In this study, we apply a novel approach to analyze COVID-19 pandemics in Greece using the SEInSRD model, shown in Fig. 1. We focus on the outbreak phases of the 4th, 5th, and 6th waves, identifying key populations and processes driving the pandemic dynamics using CSP diagnostic tools. Additionally, we explore the relationship between the system's time scales and the inflection point of the infected population. This approach allows early estimation of inflection points, aiding in predicting the plateau phase of the pandemic, as supported by previous studies [35, 36].

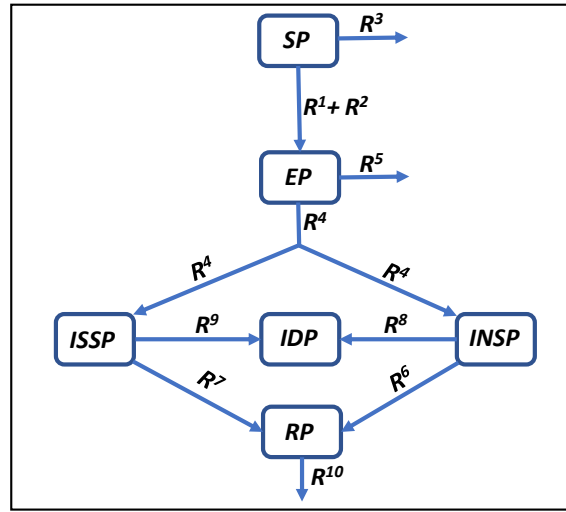


Figure 1: The SEInSRD population model employed; SP: susceptible population (not infected), EP: exposed population (infected but not yet able to infect), INSP: infected normally susceptible population (able to infect), ISSP: infected severely susceptible population (able to infect), IDP: infected dead population, RP: recovered population.  $R^i$  denotes the transmission rate of the  $i$ -th path.

## 2 Mathematical Model

In this study, the SEInSRD population model was employed, a description of which is depicted in Fig. 1. Since research indicates that COVID-19 symptoms vary from mild to severe, the SEInSRD model is an adaptation of the SEIRD model, which expands the later by splitting the infected compartment into two sub-compartments: 'normally infected' (IN) and 'severely infected' (IS) individuals. This division reflects the immediate healthcare needs of severely infected individuals and leads to the modified SEInSRD model:

$$\frac{d}{dt} \begin{bmatrix} S \\ E \\ IN \\ IS \\ R \\ D \end{bmatrix} = \begin{bmatrix} -\beta_N S.IN - \beta_S S.IS - \mu_{TP} S \\ \beta_N S.IN + \beta_S S.IS - \sigma E - \mu_{TP} E \\ (1 - ss)\sigma E - \gamma IN - \mu_N IN \\ ss\sigma E - \gamma IS - \mu_S IS \\ \gamma(IN + IS) - \mu_{TP} R \\ \mu_N IN + \mu_S IS \end{bmatrix} \quad (1)$$

where the subscripts  $N$  and  $S$  indicate the normally and severely infected transmission  $\beta$  and fatality  $\mu$  ratios,  $ss$  denotes the fraction of severely over normally infected individuals and  $\mu_{TP}$  is the physiological death ratio.

The SEInSRD model can be rewritten to its - equal to density dependent - frequency dependent formulation, as:

$$\begin{aligned}
 \dot{SP} &= -R^1 - R^2 - R^3 & \dot{EP} &= R^1 + R^2 - R^4 - R^5 \\
 \dot{INSP} &= (1 - ss)R^4 - R^6 - R^8 & \dot{ISSP} &= ssR^4 - R^7 - R^9 \\
 \dot{RP} &= R^6 + R^7 - R^{10} & \dot{IDP} &= R^8 + R^9
 \end{aligned} \tag{2}$$

where  $SP$ ,  $EP$ ,  $INSP$ ,  $ISSP$ ,  $RP$  and  $IDP$  denotes the number of susceptible, exposed, infected normally symptomatic, infected severely symptomatic, recovered and infected deceased individuals, respectively. The rates  $R^i$  are defined as:

$$\begin{aligned}
 R^1 &= \frac{\beta_{INSP}}{TP} INSP SP & R^2 &= \frac{\beta_{ISSP}}{TP} ISSP SP & R^3 &= \mu_{TP} SP \\
 R^4 &= aincp^{-1} EP & R^5 &= \mu_{TP} EP & R^6 &= aip^{-1} INSP \\
 R^7 &= aip^{-1} ISSP & R^8 &= \mu_{INSP} INSP & R^9 &= \mu_{ISSP} ISSP \\
 R^{10} &= \mu_{TP} RP
 \end{aligned}$$

where the transmission ratios are expressed in a frequency dependent representation as  $\beta_N = \beta_{INSP}/TP$  and  $\beta_S = \beta_{ISSP}/TP$ ,  $\mu_N = \mu_{INSP}$ ,  $\mu_S = \mu_{ISSP}$ ,  $\gamma = aip^{-1}$  and  $\sigma = aincp^{-1}$ . In addition, Eq. (2) yields the forming equilibration:

$$\frac{d(SP + EP + INSP + ISSP + RP + IDP)}{dt} = R^3 + R^5 + R^{10} = -\mu_{TP}(SP + EP + RP) \tag{3}$$

More details on the inflection points through analytic calculations are included in Appendix A.

### 3 Computational Singular Perturbation

The SEInSRD compartmental model of Eq. (2) can be formed as an Ordinary Differential Equation (ODE) system:

$$\frac{d\mathbf{y}}{dt} = \mathbf{g}(\mathbf{y}) = \sum_{k=1}^K \mathbf{S}_k R^k(\mathbf{y}) \tag{4}$$

where  $\mathbf{y}$  is the  $N$ -dim. column *state vector*, the elements of which are the number of individuals in the population group or their fraction over the population and  $\mathbf{g}(\mathbf{y})$  is the  $N$ -dim. column *vector field* that incorporates the transition laws from a compartmental group to another. In particular, the vector field  $\mathbf{g}(\mathbf{y})$  is described by the  $N$ -dim. stoichiometric vector  $\mathbf{S}_k$ , which indicates the direction of the  $K$  transitions from a group to another and  $R_k$ , which is the related transition rate/interaction; e.g., transmission, recovery, death rate. According to CSP, the system in Eq. (4) can be cast in the following form [8, 37]:

$$\frac{d\mathbf{y}}{dt} = \mathbf{g}(\mathbf{y}) = \sum_{n=1}^N \mathbf{a}_n(\mathbf{y}) f^n(\mathbf{y}), \quad f^n(\mathbf{y}) = \mathbf{b}^n(\mathbf{y}) \cdot \mathbf{g}(\mathbf{y}) = \sum_{k=1}^K (\mathbf{b}^n(\mathbf{y}) \cdot \mathbf{S}_k) R^k(\mathbf{y}), \tag{5}$$

where  $\mathbf{a}_n(\mathbf{y})$  and  $\mathbf{b}^n(\mathbf{y})$  are the  $N$ -dim. CSP column and row, respectively, basis vectors of the  $n$ -th mode, which satisfy the orthogonality conditions  $\mathbf{b}^i(\mathbf{y}) \cdot \mathbf{a}_j(\mathbf{y}) = \delta_j^i$  [1, 8]. In this way, the vector field  $\mathbf{g}(\mathbf{y})$  is decomposed in  $n$  CSP modes, each having a different impact in the vector field and acting in a different timescale. The impact of the  $n$ -th CSP mode is measured by the amplitude  $f^n(\mathbf{y})$  (proper adjustment of the signs of the CSP basis vectors, set  $f^n(\mathbf{y})$  always positive), which provides a measure of the projection of the vector field  $\mathbf{g}(\mathbf{y})$  on the CSP vector  $\mathbf{a}_n$ . When the system in Eq. (5) exhibits  $M$  timescales that are [i] of dissipative nature (i.e., when the components of the system that generate them tend to drive the system towards equilibrium) and [ii] much faster than the rest, the model can be reduced in:

$$f^r(\mathbf{y}) \approx 0 \quad (r = 1, \dots, M), \quad \frac{d\mathbf{y}}{dt} \approx \sum_{s=M+1}^N \mathbf{a}_s(\mathbf{y}) f^s(\mathbf{y}), \tag{6}$$

the first relation of which is an  $M$ -dim. system of algebraic equations defining the manifold  $\mathcal{M}$  (a low dimensional surface in phase-space, where the system is confined to evolve), while the second relation is an  $N$ -dim. system of ODEs

governing the slow evolution of the system on this manifold. The objective of asymptotic analysis techniques is to deliver the expressions in Eq. (6), which are provided, order by order, by CSP in algorithmic fashion [38, 39]. This is accomplished through the CSP vectors,  $\mathbf{a}_i(\mathbf{y})$  and  $\mathbf{b}^i(\mathbf{y})$  ( $i = 1, \dots, N$ ), which can be approximated in leading order accuracy by the right and left, respectively, eigenvectors of the  $N \times N$ -dim. Jacobian  $\mathbf{J}(\mathbf{y})$  of  $\mathbf{g}(\mathbf{y})$ ; i.e.,  $\mathbf{a}_i(\mathbf{y}) = \alpha_i(\mathbf{y})$  and  $\mathbf{b}^i(\mathbf{y}) = \beta^i(\mathbf{y})$  [8, 37, 40]. In the following, for simplicity reasons, the dependency of  $R^k$ ,  $\mathbf{g}$ ,  $\alpha$ , etc, to  $\mathbf{y}$  will be removed, and be mentioned only when explicitly needed.

The interactions among the population groups have a different impact to the evolution of the system, either to the constraints along which the system is confined to evolve or to its slow evolution along them. In particular, the  $M$  constraints in Eq. (6)  $f^r = (\beta^r \cdot \mathbf{S}_1)R^1 + \dots + (\beta^r \cdot \mathbf{S}_K)R^K \approx 0$  ( $r = 1, \dots, M$ ) result from significant cancellations among some of the additive terms  $(\beta^r \cdot \mathbf{S}_k)R^k$  ( $k = 1, \dots, K$ ). In addition, the slow evolution of the system is characterized by the slow CSP modes, the impact of which is measured by the slow amplitudes  $f^s$  in Eq. (6). The interactions that contribute significantly to (i) the formation of each of the  $M$  constraints and (ii) the governing components of the slow system, are identified by the *Amplitude Participation Index (API)*:

$$P_k^n = \frac{(\beta^n \mathbf{S}_k)R^k}{\sum_{i=1}^K |(\beta^n \mathbf{S}_i)R^i|} \quad (k = 1, \dots, K), \quad (7)$$

where by definition  $\sum_{k=1}^K |P_k^n| = 1$  [1, 41, 42]. When employed to the fast  $r = 1, \dots, M$  CSP modes,  $P_k^r$  measures the relative contribution of the  $k$ -th interaction to the cancellations among the additive terms in  $f^r \approx 0$ , while when employed to the slow  $s = M + 1, \dots, N$  CSP modes,  $P_k^s$  measures the relative contribution of the  $k$ -th interaction to governing slow system. Both  $P_k^r$  and  $P_k^s$  can be either positive or negative; the sum of positive and negative  $P_k^r$  terms equaling 0.5, by definition [43–46].

The formation of the  $M$  constraints is characterized by the  $M$  fastest timescales, which by definition are of dissipative nature; see requirement [i] immediately before Eq. (6). On the contrary, the dynamics of the slow system in Eq. (6) is characterized either by the fastest of the  $N - M$  dissipative slow timescales or by explosive timescales, when the later are present, since they tend to drive the system away from equilibrium. The timescales are approximated by the inverse of the eigenvalues of the Jacobian  $\mathbf{J}$ ,  $\tau_n = |\lambda_n|^{-1}$  ( $n = 1, \dots, N$ ). The CSP diagnostic tool, *Timescale Participation Index (TPI)*, identifies the reactions significantly contributing to the generation of the timescales:

$$J_k^n = \frac{c_k^n}{\sum_{i=1}^K |c_i^n|} \quad (k = 1, \dots, K), \quad (8)$$

where  $\lambda_n = c_1^n + \dots + c_K^n$  and by definition  $\sum_{k=1}^K |J_k^n| = 1$  [41, 47, 48].  $c_k^n$  denotes the contribution of the  $k$ -th interaction to the  $n$ -th eigenvalue and can be calculated as  $c_k^n = \beta^n \nabla(\mathbf{S}_k R^k) \alpha_n$ , where  $\sum_{k=1}^K \nabla(\mathbf{S}_k R^k)$  is the Jacobian  $\mathbf{J}$ .  $c_k^n$  can be either positive or negative and therefore, a negative (positive)  $J_k^n$  implies that the  $k$ -th interaction contributes to a dissipative (explosive) character of the  $n$ -th timescale  $\tau_n$  [49, 50]. By definition, dissipative (explosive) timescales relate to the components of the system that tend to drive it towards (away from) equilibrium [1, 8]. TPI has been successfully used

Each population group/compartment is associated differently to each CSP mode; e.g., a fast CSP mode is expected to be much more related to the infected compartment than the recovered one, since the former are playing a major role as opposed to the latter at the beginning of an epidemics. The relation of the  $m$ -th CSP mode ( $m = 1, \dots, M$ ) to the various population groups is identified by the *Pointer (Po)*:

$$\mathbf{D}^m = \text{diag}[\alpha_m \beta^m] = [\alpha_m^1 \beta_1^m, \alpha_m^2 \beta_2^m, \dots, \alpha_m^N \beta_N^m] \quad (m = 1, \dots, M), \quad (9)$$

where, due to the orthogonality condition  $\beta^i \cdot \alpha_j = \delta_j^i$ , the sum of all  $N$  elements of  $\mathbf{D}^m$  equals unity, i.e.  $\sum_{i=1}^N \alpha_m^i \beta_i^m = 1$  [1, 3, 42, 51]. A relatively large value of  $\alpha_m^i \beta_i^m$  indicates that the  $i$ -th population group is strongly associated to  $m$ -th CSP mode and the  $m$ -th timescale. A value of  $D_i^m$  close to unity suggests that the  $i$ -th population group is in *Quasi Steady-State (QSS)* [51].

## 4 Results

The fastest of the *explosive time scales* in the dynamics of the process characterises the *outbreak phase* from the start of the process, up to the point where these time scales cease to exist (this is the period in which the system accelerates at the start of the outbreak phase) and that the remaining period of this phase is characterised by the fastest of the *dissipative time scales* (this is the period in which the system decelerates as it approaches the end of the outbreak phase, known as the *peak*). The transition from the accelerating to the decelerating period, defines the *inflection point* in the

profile of the active cases, during the *outbreak phase*. The development of the *inflection point* is an early warning that the *peak* will be reached soon.

The explosive and dissipative time scales that characterize the outbreak phase were computed by fitting the available data (from Worldometer database, number of exposed, infected and dead) to the SEInSRD model, shown in Fig. 1.

#### 4.1 The 4th wave

In this section, results for the 4th wave will be presented. For validation purposes, the analysis was done by considering solutions obtained by fitting data from two periods in 2021:

- i) Period A, July 1 - July 8, 8 days long,
- ii) Period B, July 1 - July 18, 18 days long,

where July 1 marks the start of the 4th wave.

The evolution of the active cases from the Worldometer database are shown in Fig. 2 with circles (up to 12/8/21). In addition, Fig. 2 displays the number of active cases, as it was computed from the SEInSRD model, when fitted to Period A (8 days long) and Period B (18 days long) data.

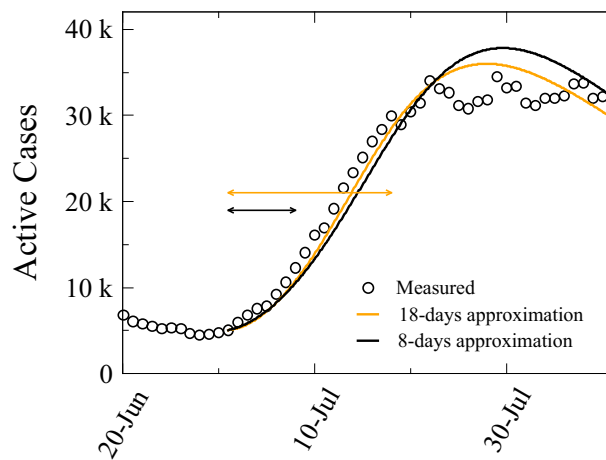


Figure 2: The active cases (INSP+ISSP, see Fig. 1) according to the available data (circles) and the solution of the SEInSRD model (curves), fitted to Period A (July 1-8) and Period B (July 1-18) data. The two periods are shown with horizontal arrows.

The *explosive* and *dissipative* (attenuating) time scales that characterise the dynamics in the outbreak phase are shown in Fig. 3. The *fast explosive* time scale characterises the evolution of the process, from July 1st until the day when this time scale ceases to exist; i.e., July 14 according to Period A and July 12 according to period B.

According to the profiles shown in Fig. 2, the *inflection point* in the profile of the active cases was manifested on July 15 and July 13, according to the solutions based on data spanning Period A and Period B, respectively. These two days are approximated very well by the days in which the *explosive* time scales disappear; i.e., July 14 and July 12 for the two periods, as shown in Fig. 3. The disappearance of the *explosive* time scales is preceded by their coalescence, as shown in Fig. 3; July 9 for Period A and July 8 for Period B. According to these findings, by July 8-9 it was possible to predict that the development of a peak (plateau in this case) was imminent.

Given the significance of the *fast explosive* time scale (the faster this scale the more intense the outbreak), it is of interest to identify the paths of the model in Fig. 1, which either promote or oppose its appearance. The results displayed in Table 1 suggest that the intensity of the initiation of the outbreak is mainly promoted by Paths 1 and 4 (susceptible becoming exposed and then infected), while it is opposed by Path 6 (infected becoming recovered). In addition, it is shown that - as the end of the explosive period is reached - the promoting influence of Paths 1 and 4 diminishes, while the opposing one of Path 6 increases (doubles).

The analysis of available data extending in the period July 1-8 produced similar results with the analysis of data extending in the period July 1-18. By concentrating on the inflection point in the profile of active cases, it was shown

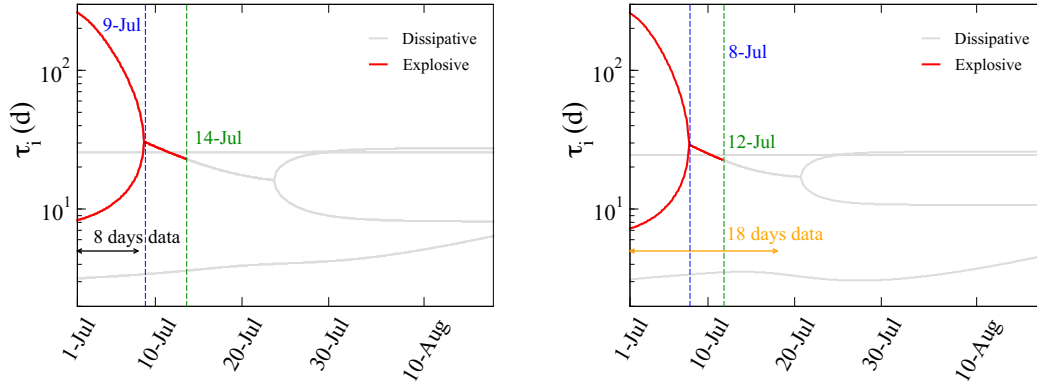


Figure 3: The explosive (in red) and dissipative (attenuating, in gray) time scales; profiles based by fitting data from Period A (8 days) and Period B (18 days). The vertical blue dashed line denotes the point where the two explosive time scales coalesce, indicating that their disappearance is imminent. The vertical green dashed line denotes the point where the explosive time scales disappear. The fastest explosive time scale characterises the initial part of the outbreak phase and the fastest dissipative (attenuating) time scale characterises the remaining part.

Table 1: The percentage contribution of the various paths to the development of the fastest explosive time scale, estimated on July 1 and 7.

Path	Period A solution		Path	Period B solution	
	July 1	July 7		July 1	July 7
$R^1$	51.8%	43.8%	$R^1$	47.6%	35.1%
$R^4$	32.6%	28.9%	$R^4$	38.3%	33.4%
$R^6$	-14.8%	-26.3%	$R^6$	-13.6%	-30.3%

that **we could know on July 8 or 9 - the latest** - that the peak of active cases was within reach (eventually it was recorded around July 22). Finally, it was shown that it is possible to **quantify**, the degree to which the intensity and duration of the *outbreak phase* can be controlled by decreasing the rate by which susceptible become infected and by increasing the rate by which infected become recovered.

## 4.2 The 5th wave

In this section, results for the 5th wave will be presented. For validation purposes, the analysis was done by considering solutions obtained by fitting data from two periods in 2021:

- i) Period C, October 10 - October 23, 14 days long,
- ii) Period D, October 10 - November 6, 28 days long,

where October 10 marks the start of the 5th wave.

The evolution of the active cases from the Worldometer database are shown in Fig. 4 with circles (up to 23/11/21). In addition, Fig. 4 displays the number of active cases, as it was computed from the SEInSRD model, when fitted to Period C (14 days long) and Period D (28 days long) data; the extend of the two periods shown in Fig. 4.

The *explosive* and *dissipative* (attenuating) time scales that characterise the dynamics in the outbreak phase are shown in Fig. 7. The *fast explosive* time scale is present from the assumed start of the 5th wave in October 10, until 2 January 2022 according to the Period C data and 26 December 2021 according to Period D data. Since the influence of the fast explosive time scale weakens after it meets the slow one (21-22 November), it is expected that the inflection point of the infected population will manifest early in December.

Similarly to 4th wave, it is of interest to identify the paths of the model in Fig. 1, which either promote or oppose the generation of the *fast explosive* time scale. The results displayed in Table 2 suggest that the intensity of the initiation of this outbreak is mainly promoted by Paths 1 and 4 (susceptible becoming exposed and then infected), while it is opposed by Path 6 (infected becoming recovered). It is shown that over a 2-weeks period from the start of the 5th wave, there are no significant changes in the major contributions from paths 1, 4 and 6. This is in contrast to the 4th wave (see

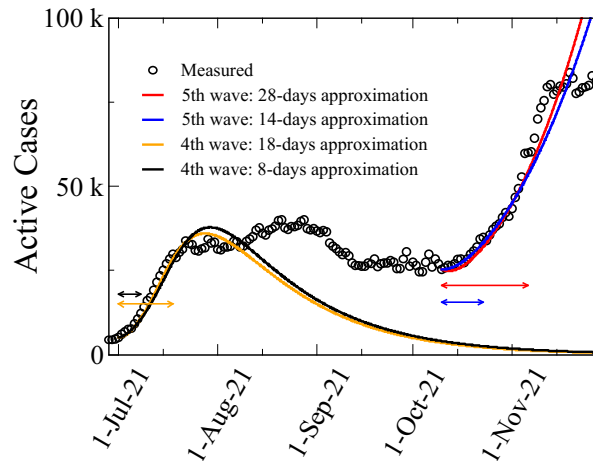


Figure 4: The active cases (INSP+ISSP, see Fig. 1) according to the available data (circles) and the solution of the SEInSRD model (curves), fitted to Period C (October 10 - 23) and Period D (October 10 - November 6) data. The two periods are shown with horizontal arrows. For comparison, the solution of the model fitted to Periods A and B are displayed.

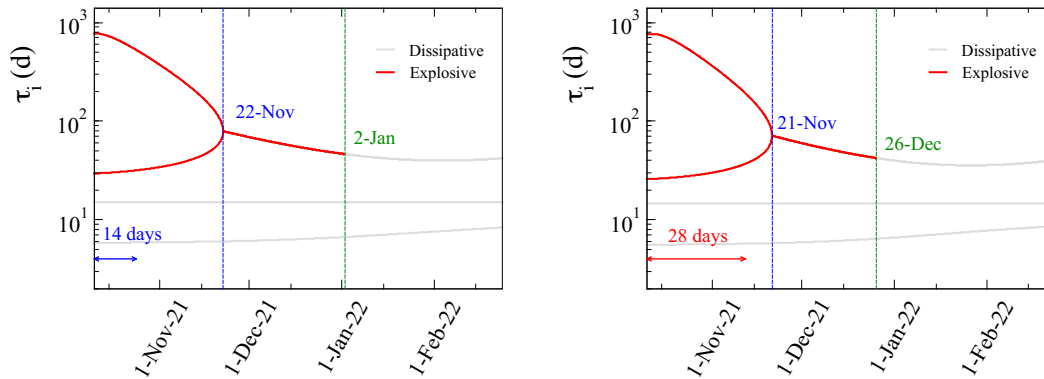


Figure 5: The explosive (in red) and dissipative (attenuating, in gray) time scales; profiles based by fitting data from Period C (14 days) and Period D (28 days). The vertical blue dashed line denotes the point where the two explosive time scales coalesce, indicating that their disappearance is imminent. The vertical green dashed line denotes the point where the explosive time scales disappear. The fastest explosive time scale characterises the initial part of the outbreak phase and the fastest dissipative (attenuating) time scale characterises the remaining part.

Table 1), where over a 1-week period from the start there was a significant decrease in the promoting to the explosive stage contribution of Paths 1 and 4 and a significant increase in the opposing contribution of Path 6. This feature is related to the expectation that the duration of the 5th wave will be longer than that of the 4th one; see Section 5.

In addition, a comparison of Tables 1 and 2 reveals that the opposing to the explosive time scale influence of Path 6 (infected becoming recovered) is much stronger in wave 5 (about -33% during the first two weeks of the outbreak) than in wave 4 (about -15% at the start of the wave to about -30% a week later).

The analysis of available data extending in the period October 10-23 produced qualitatively similar results with the analysis of data extending in the period October 10 - November 6. Both periods predict the development of an inflection point (the point where the increase of active cases stops accelerating and starts decelerating) early in December.

*Although the explosive period during the 5th wave is longer than that during the 4th wave, the opposing Path 6 (infected population becoming recovered one) is stronger in the 5th wave from its start, most likely due to the larger portion of vaccinated people in the infected population. Consequently, if this opposing factor had not being so strong, the promoting influence of Paths 1 and 4 (susceptible population becoming exposed and then infected one) would have*

Table 2: The percentage contribution of the various paths to the development of the fastest explosive time scale, estimated on October 10 and 24.

Path	Period C solution		Path	Period D solution	
	October 10	October 24		October 10	October 24
$R^1$	48.9%	48.4%	$R^1$	48.9%	48.5%
$R^6$	-33.4%	-34.5%	$R^6$	-32.2%	-33.2%
$R^4$	17.1%	16.5%	$R^4$	18.3%	17.7%

made the outbreak phase even stronger. As in the 4th wave, this opposing influence of Path 6 is expected to grow further towards the end of the explosive period.

### 4.3 The 6th wave

In this section, results for the 6th wave will be presented. The analysis was done by considering a solution obtained by fitting data from a period of ten days, say Period E, from 26 December 2021 to 4 January 2022, where 26 December 2021 marks the start of the 6th wave.

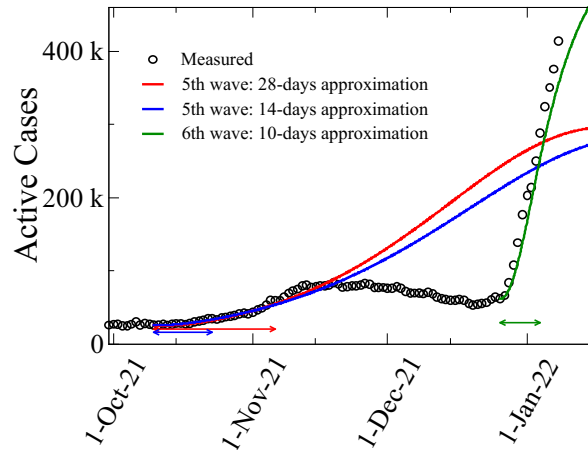


Figure 6: The active cases (INSP+ISSP, see Fig. 1) according to the available data (circles) and the solution of the SEInSRD model (curves), fitted to Period E (December 26 '21- January 4 '22) data. For comparison, the solution of the model fitted to Periods C and D are displayed. The various periods are shown with horizontal arrows.

The evolution of the active cases from the Worldometer database are shown in Fig. 6 with circles (up to 08/01/22), along with the number of active cases, as it was computed from the SEInSRD model, when fitted to the Period E data.

The *explosive* and *dissipative* (attenuating) time scales that characterise the dynamics in the outbreak phase are shown in Fig. 7. The *fast explosive* time scale is present from the assumed start of the 6th wave in December 26 until 31 December 2021. Since the influence of the fast explosive time scale weakens after it meets the slow one (30 December), it is expected that the inflection point of the infected population will manifest the first days of January 2022.

The use of the CSP tools reveals the paths that affect the generation of the *fast explosive* time scale. The results displayed in Table 3 suggest that the intensity of the initiation of this outbreak is mainly promoted by Path 4 (exposed becoming effected) and in a lesser degree by Path 1 (susceptible becoming exposed), while it is opposed by Path 6 (infected becoming recovered).

According the Table 3, during the outbreak of the 6th wave, the relevant contributions of the main paths do not change much. Furthermore, it is shown that the opposing to the explosive time scale influence of Path 6 (infected becoming recovered) is much more weaker in the 6th wave, compared to the one of both waves 4 and 5; see Tables 1 and 2.

The analysis of available data extending in the period 26 December 2021 to 4 January 2022 predicted the development of an inflection point of active cases (the point where the increase of cases stops accelerating and starts decelerating) early in January. This implies that the relaxation period (decrease of active cases) will initiate soon.

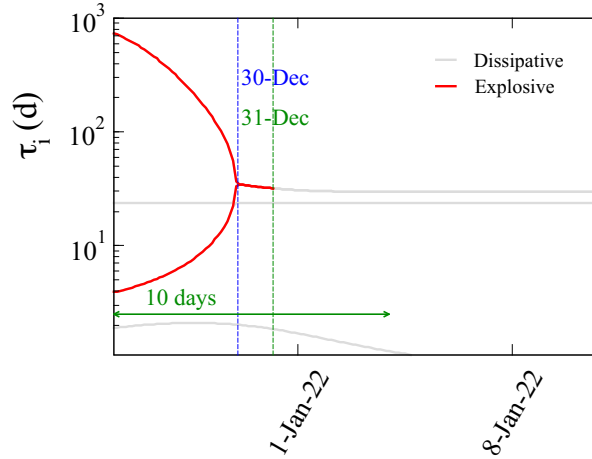


Figure 7: The explosive (in red) and dissipative (attenuating, in gray) time scales; profiles based by fitting data from Period E (10 days). The vertical blue dashed line denotes the point where the two explosive time scales coalesce, indicating that their disappearance is imminent. The vertical green dashed line denotes the point where the explosive time scales disappear. The fastest explosive time scale characterises the initial part of the outbreak phase and the fastest implosive (dissipative) time scale characterises the remaining part.

Table 3: The percentage contribution of the various paths to the development of the fastest explosive time scale, estimated on December 26 and 28.

Path	Period E solution	
	December 26	December 28
$R^4$	56.8%	59.1%
$R^1$	35.6%	28.6%
$R^6$	-7.4%	-11.9%

In contrast to the case of the 4th and 5th waves, the promoting the outbreak phase influence of Path 4 (exposed population becoming infected) was more significant than that of Path 1 (susceptible population becoming exposed), confirming the wider dispersion of the omicron variant to the general population

It was also shown that the opposing influence of Path 6 (infected population becoming recovered one) is very small; smaller than in the 4th and 5th waves, most likely due to the weaker effects of the vaccines when dealing with the omicron variant.

## 5 Comparison between waves 4, 5 and 6

Tables 4 and 5 allow for a direct comparison of the dynamics of the three outbreak phases and the origin of their differences.

Table 4 lists the explosive time scale  $\tau$  at the start of the outbreak phase and at the point where this time scale disappears; the latter coinciding with the inflection point of the active cases. It is shown that  $\tau$  is about 8 d, 28 d and 4 d at the start of the outbreak phase in the case of the 4th, 5th and 6th waves, respectively. This implies that the process is twice as fast at the start of the outbreak phase of the 6th wave in comparison to that of the 4th wave and seven times as fast in comparison to that of the 5th wave. Regarding the point where the fast time scale disappears, the 4th and 6th waves are equally fast and about twice as fast in comparison to the 5th wave.

Table 5 lists the contributions of the various paths of the model employed to the explosive time scale at the start of the outbreak in each wave considered. The two major findings are (i) the switch from the non-infected population to the exposed one, as the population contributing the most to the outbreak phase, which confirms the wider dispersion of the omicron variant to the general population and (ii) the weaker opposition to the outbreak phase in the 6th wave relative to the 5th one (the first dominated by the omicron variant and the latter by the delta one), which is in accordance to the

Table 4: Comparison between the developing explosive time scales of the 4th, 5th and 6th waves.  $\tau_e^0$  and  $\tau_e^{end}$  represent the value of the fast explosive time scale at the start of each wave and at the time when the explosive modes disappear, respectively.

Wave 4		Wave 5		Wave 6
Period A	Period B	Period C	Period D	Period E
$\tau_{e,A}^0 = 8.33$ d	$\tau_{e,B}^0 = 7.24$ d	$\tau_{e,C}^0 = 29.5$ d	$\tau_{e,D}^0 = 25.89$ d	$\tau_{e,E}^0 = 3.8$ d
$\tau_{e,A}^{end} = 30.53$ d	$\tau_{e,B}^{end} = 29.14$ d	$\tau_{e,C}^{end} = 78.7$ d	$\tau_{e,D}^{end} = 71.1$ d	$\tau_{e,E}^{end} = 34.9$ d

Table 5: Comparison between the major contributors to the explosive time scale at the initiation of the 4th, 5th and 6th waves.

Wave 4	Wave 5	Wave 6
$R^1$ : $\sim 50\%$	$R^1$ : $\sim 49\%$	$R^4$ : $\sim 59\%$
$R^4$ : $\sim 36\%$	$R^6$ : $\sim 33\%$	$R^1$ : $\sim 29\%$
$R^6$ : $\sim 14\%$	$R^4$ : $\sim 18\%$	$R^6$ : $\sim 12\%$

higher infection rate due to the omicron variant and the decreased efficiency of the vaccines when dealing with this variant..

## 6 Conclusions

Results based on an alternative and robust methodology for predicting the evolution of each COVID-19 wave were presented. The methodology focuses on the *fast explosive* time scale that characterises the intensity and duration of the *outbreak phase*. The point where this time scale ceases to characterize the process coincides with the inflection point of active cases; the point where the increase of active cases stops accelerating and starts decelerating. Since the inflection point precedes the peak, this methodology serves as an early warning of the peak. In addition, this methodology allows for the identification of the factors (paths) that can influence the intensity and length of the *outbreak phase*.

The last major three epidemic waves were analyzed, as they were recorded in the periods 1.7.2021-9.10.2021 (4th wave), 10.10.2021-19.12.2021 (5th wave) and 20.12.2021-today (6th wave, still developing); the first two periods dominated by the *delta* variant of the virus and the last one by the *omicron* variant. By examining the dynamics of their *outbreak phase*, it is concluded that:

- i) The most intense *outbreak phase* is that of the 6th wave, followed by that of the 4th wave; the one of the 5th wave being by far the least intense. This finding confirms (i) *the dominance of the omicron variant, relative to the delta one*, (ii) *the relaxing influence of vaccinations* (much higher percentage of vaccinated population during the 5th wave relative to the 4th and not significant difference between the 5th and the 6th waves) and (iii) the weak influence of vaccines when dealing with the omicron variant.
- ii) The major contribution to the *outbreak phase* of the 4th and 5th waves originates from the non-infected population becoming exposed (infected but not yet able to transmit the virus), followed by the exposed population becoming infected (able to infect). In the 6th wave, this ordering is reversed, so that the population group dominating the *outbreak phase* is the exposed population and not the non-infected ones of the 4th and 5th waves. This switch *confirms the wider dispersion of the omicron variant in the general population*.
- iii) The major opposing influence to the intensity of the *outbreak phase* of all three waves originates from the infected population becoming recovered. This opposition is strongest in the 5th wave (least intense wave) and weakest in the 6th wave (most intense wave).
  - a) The stronger opposition to the *outbreak phase* in the 5th wave relative to the 4th one (both dominated by the delta variant) is *in accordance to the higher vaccinated percentage of the general population during the 5th wave*.
  - b) The weaker opposition to the *outbreak phase* in the 6th wave relative to the 5th one (the first dominated by the omicron variant and the latter by the delta one) is *in accordance to the higher infection rate due to the omicron variant and the decreased efficiency of the vaccines when dealing with this variant*.
- iv) The inflection point of active cases in the current 6th wave occurred in the first days of January 2022, so the outbreak is about to start relaxing.

**NOTE 1:** The predictions reported here for the 4th wave were based on the prevailing conditions in Periods A (July 1-8) and B (July 1-18). It was demonstrated that it was possible to predict by July 8 or 9 - the latest - that the peak of active cases was within reach; eventually, it was recorded around July 22.

The predictions reported for the 5th wave are valid under the assumption that the prevailing conditions in Periods C (October 10-23) and D (October 10 - November 6) keep prevailing in the period that follows.

Similarly, the predictions reported for the 6th wave are valid under the assumption that the prevailing conditions in Periods E (26 December 2021 to 4 January 2022) keep prevailing in the period that follows.

**NOTE 2:** In accordance to recent studies, it is assumed here that the probability of transmission between vaccinated or not-vaccinated does not differ significantly.

## A Appendix

According to the frequency dependent representation of SEInSRD model in Eq. (2), the following conclusions can be drawn, regarding to the inflection points  $SP$ ,  $EP$ ,  $INSP$  and  $ISSP$ , through analytic calculations.

### A.1 Inflection point of SP close to max $R^1$ and $R^2$

Differentiation of the SP differential equation in Eq. (2) yields:

$$\dot{S}P = -\dot{R}^1 - \dot{R}^2 - \dot{R}^3 = -(\dot{R}^1 + \dot{R}^2) + \mu_{TP}(R^1 + R^2 + R^3) \quad (10)$$

Neglecting the terms  $\mu_{TP}(R^1 + R^2 + R^3)$ , since  $\mu_{TP} \ll 1$ , yields:

$$\dot{S}P \approx -(\dot{R}^1 + \dot{R}^2) \quad (11)$$

During the explosive stage both  $R^1$  and  $R^2$  increase with time; i.e. initially the rate by which  $SP$  gets infected increases with time ( $\dot{S}P < 0$  and  $\ddot{S}P < 0$ ). According to Eq. (11), an inflection point of  $SP$  ( $\ddot{S}P = 0$ ) might occur when  $R^1$  and  $R^2$  attain their maximum values ( $\dot{R}^1 = \dot{R}^2 = 0$ ). The inflection point of  $SP$  and the points in time where  $R^1$  and  $R^2$  attain their maximum values are indeed very close. The differences are related to the magnitude of the term  $\mu_{TP}(R^1 + R^2 + R^3)$ .

### A.2 Inflection points of SP and EP

Differentiation of the sum of SP and EP equations in Eq. (2) yields:

$$\ddot{S}P + \ddot{E}P = -\dot{R}^3 - \dot{R}^4 - \dot{R}^5 = -\frac{\dot{E}P}{aincp} - \mu_{TP}(\dot{S}P + \dot{E}P) \quad (12)$$

Neglecting the terms  $\mu_{TP}(\dot{S}P + \dot{E}P)$ , since  $\mu_{TP} \ll 1$ , yields:

$$\ddot{S}P + \ddot{E}P \approx -\frac{1}{aincp}\dot{E}P \quad (13)$$

Given that  $\dot{E}P > 0$  during the explosive stage, Eq. (13) indicates that  $\ddot{S}P + \ddot{E}P < 0$  there. In addition, with the exception of the very early and very late parts of the explosive stage,  $\dot{S}P \leq 0$  and  $\dot{E}P \geq 0$  throughout this stage; i.e., the rate of increase of  $EP$  and the rate of decrease of  $SP$  intensify. Moving towards the end of the explosive stage,  $\dot{E}P$  decreases, being reflected with a drop of the increasing trend of  $EP$ . At the end of the explosive stage,  $\dot{E}P$  attains small positive values, so that Eq. (13) yields that the inflection point of  $EP$  ( $\ddot{E}P = 0$ ) comes shortly before the end of the explosive stage, followed by the inflection point of  $SP$  ( $\dot{S}P = 0$ ).

### A.3 Inflection points of INSP and ISSP coinciding with max $R^4$

Differentiation of the sum of INSP and ISSP equations in Eq. (2) yields:

$$\begin{aligned} IN\ddot{S}P + IS\ddot{S}P &= \dot{R}^4 - \dot{R}^6 - \dot{R}^7 - \dot{R}^8 - \dot{R}^9 \\ &= \frac{\dot{E}P}{aincp} - \left( \frac{1}{aip} + \mu_{INSP} \right) IN\dot{S}P - \left( \frac{1}{aip} + \mu_{ISSP} \right) IS\dot{S}P \end{aligned} \quad (14)$$

The summation of all the differential equations in Eq. (2) yields:

$$\dot{S}P + \dot{E}P + \dot{I}NSP + \dot{I}SSP + \dot{R}P + \dot{I}DP = -R^3 - R^5 - R^{10} = \quad (15)$$

in which the terms  $\dot{R}P$ ,  $\dot{I}DP$  and  $-R^3 - R^5 - R^{10}$  are very small during the explosive stage, such that:

$$\dot{S}P + \dot{E}P + \dot{I}NSP + \dot{I}SSP = 0 \quad (16)$$

Differentiation of Eq. (16) yields:

$$\ddot{S}P + \ddot{E}P + \ddot{I}NSP + \ddot{I}SSP = 0 \quad (17)$$

which, after algebraic calculations, takes the form:

$$\mu_{TP}(\dot{S}P + \dot{E}P) + \left(\frac{1}{aip} + \mu_{INSP}\right) \dot{I}NSP + \left(\frac{1}{aip} + \mu_{ISSP}\right) \dot{I}SSP = 0 \quad (18)$$

Differentiation of Eq. (18) implies:

$$\mu_{TP}(\ddot{S}P + \ddot{E}P) + \left(\frac{1}{aip} + \mu_{INSP}\right) \ddot{I}NSP + \left(\frac{1}{aip} + \mu_{ISSP}\right) \ddot{I}SSP = 0 \quad (19)$$

in which the substitution of Eq. (13) yields:

$$-\left(\mu_{TP}^2 + \frac{\mu_{TP}}{aincp}\right) \dot{E}P + \left(\frac{1}{aip} + \mu_{INSP}\right) \ddot{I}NSP + \left(\frac{1}{aip} + \mu_{ISSP}\right) \ddot{I}SSP = 0 \quad (20)$$

Given that  $\dot{E}P > 0$ ,  $\ddot{I}NSP > 0$  and  $\ddot{I}SSP > 0$  during the explosive stage and that  $\dot{I}NSP$  and  $\dot{I}SSP$  attain small positive values, when moving towards to the end of it, Eq. (20) denotes that the inflection points of INSP and ISSP ( $\ddot{I}NSP \approx \ddot{I}SSP = 0$ ) coincide with the time point at which EP attains its maximum value ( $\dot{E}P = 0$ ).

## References

- [1] S. H. Lam and D. A. Goussis. The csp method for simplifying kinetics. *International journal of chemical kinetics*, 26(4):461–486, 1994.
- [2] SH Lam and DA Goussis. The csp method for simplifying kinetics. *International journal of chemical kinetics*, 26(4):461–486, 1994.
- [3] D.A. Goussis and S.H. Lam. A study of homogeneous methanol oxidation kinetics using csp. In *Symposium (International) on Combustion*, volume 24, pages 113–120. Elsevier, 1992.
- [4] Mauro Valorani, Habib N Najm, and Dimitris A Goussis. Csp analysis of a transient flame-vortex interaction: time scales and manifolds. *Combustion and Flame*, 134(1-2):35–53, 2003.
- [5] Dimitris A Goussis. The role of slow system dynamics in predicting the degeneracy of slow invariant manifolds: the case of vdp relaxation–oscillations. *Physica D: Nonlinear Phenomena*, 248:16–32, 2013.
- [6] Dimitris T Maris and Dimitris A Goussis. The “hidden” dynamics of the rössler attractor. *Physica D: Nonlinear Phenomena*, 295:66–90, 2015.
- [7] Dimitrios G Patsatzis, Gianluca Fabiani, Lucia Russo, and Constantinos Siettos. Slow invariant manifolds of singularly perturbed systems via physics-informed machine learning. *arXiv preprint arXiv:2309.07946*, 2023.
- [8] S.H. Lam and D.A. Goussis. Understanding complex chemical kinetics with computational singular perturbation. In *Symposium (International) on Combustion*, volume 22, pages 931–941. Elsevier, 1989.
- [9] M Hadjinicolaou and D A Goussis. Asymptotic solution of stiff PDEs with the CSP method: the reaction diffusion equation. *SIAM J. Sci. Comput.*, 20:781–810, 1998.
- [10] Dimitris M Manias, Efstathios Al Tingas, Christos E Frouzakis, Konstantinos Boulouchos, and Dimitris A Goussis. The mechanism by which ch2o and h2o2 additives affect the autoignition of ch4/air mixtures. *Combustion and Flame*, 164:111–125, 2016.
- [11] Shahid Rabbani, Dimitris M Manias, Dimitrios C Kyritsis, and Dimitris A Goussis. Comparative review of the chemical dynamics underlying five models of ammonia fuel oxidation. *Fuel*, 352:129063, 2023.
- [12] Shahid Rabbani, Dimitris M Manias, Dimitrios C Kyritsis, and Dimitris A Goussis. Dominant dynamics of n-butanol/air autoignition and the influence of additives. *Combustion and Flame*, 242:112173, 2022.

- [13] Shahid Rabbani, Dimitris M Manias, Dimitrios C Kyritsis, and Dimitris A Goussis. Chemical dynamics of the autoignition of near-stoichiometric and rich methanol/air mixtures. *Combustion Theory and Modelling*, Accepted: 1–31, 2021.
- [14] Dimitris M Manias, Dimitris G Patsatzis, Dimitrios C Kyritsis, and Dimitris A Goussis.  $\text{NH}_3$  vs.  $\text{CH}_4$  autoignition: A comparison of chemical dynamics. *Combustion Theory and Modelling*, 25(6):1110–1131, 2021.
- [15] Dimitris M Manias, Aliou Sow, Efstathios-Al Tingas, Francisco E Hernandez Perez, Hong G Im, and Dimitris A Goussis. Mechanism of cold-spot autoignition in a hydrogen/air mixture. *arXiv preprint arXiv:2210.06953*, 2022.
- [16] Ahmed T Khalil, Dimitris M Manias, Dimitrios C Kyritsis, and Dimitris A Goussis. No formation and autoignition dynamics during combustion of  $\text{H}_2\text{O}$ -diluted  $\text{NH}_3/\text{H}_2\text{O}_2$  mixtures with air. *Energies*, 14(1):84, 2021.
- [17] Ahmed T Khalil, Dimitris M Manias, Efstathios-Al Tingas, Dimitrios C Kyritsis, and Dimitris A Goussis. Algorithmic analysis of chemical dynamics of the autoignition of  $\text{NH}_3$ - $\text{H}_2\text{O}_2$ /air mixtures. *Energies*, 12(23):4422, 2019.
- [18] Efstathios Al Tingas, Dimitris M Manias, S Mani Sarathy, and Dimitris A Goussis.  $\text{CH}_4$ /air homogeneous autoignition: A comparison of two chemical kinetics mechanisms. *Fuel*, 223:74–85, 2018.
- [19] Dimitris G Patsatzis and Dimitris A Goussis. A new michaelis-menten equation valid everywhere multi-scale dynamics prevails. *Mathematical biosciences*, 315:108220, 2019.
- [20] Dimitris G Patsatzis, Dimitris T Maris, and Dimitris A Goussis. Asymptotic analysis of a target-mediated drug disposition model: algorithmic and traditional approaches. *Bulletin of mathematical biology*, 78(6):1121–1161, 2016.
- [21] Dimitrios G Patsatzis. Algorithmic asymptotic analysis: Extending the arsenal of cancer immunology modeling. *Journal of Theoretical Biology*, 534:110975, 2022.
- [22] Sébastien Gaucel, Béatrice Laroche, Pauline Ezanno, Elisabeta Vergu, and Suzanne Touzeau. Using singular perturbations to reduce an epidemiological model: Application to bovine viral diarrhoea virus within-herd spread. *Journal of theoretical biology*, 258(3):426–436, 2009.
- [23] Fred Brauer. A singular perturbation approach to epidemics of vector-transmitted diseases. *Infectious Disease Modelling*, 4:115–123, 2019.
- [24] Max O Souza. Multiscale analysis for a vector-borne epidemic model. *Journal of mathematical biology*, 68:1269–1293, 2014.
- [25] Zhonghua Zhang, Yaohong Suo, Jigen Peng, and Weihua Lin. Singular perturbation approach to stability of a sirs epidemic system. *Nonlinear Analysis: Real World Applications*, 10(5):2688–2699, 2009.
- [26] Hildeberto Jardón-Kojakhmetov, Christian Kuehn, Andrea Pugliese, and Mattia Sensi. A geometric analysis of the sir, sirs and sirws epidemiological models. *Nonlinear Analysis: Real World Applications*, 58:103220, 2021.
- [27] Gerardo Chowell, Santiago Echevarría-Zuno, Cecile Viboud, Lone Simonsen, James Tamerius, Mark A Miller, and Víctor H Borja-Aburto. Characterizing the epidemiology of the 2009 influenza a/h1n1 pandemic in mexico. *PLoS Med*, 8(5):e1000436, 2011.
- [28] Jacco Wallinga and Marc Lipsitch. How generation intervals shape the relationship between growth rates and reproductive numbers. *Proceedings of the Royal Society B: Biological Sciences*, 274(1609):599–604, 2007.
- [29] Sang Woo Park, David Champredon, Joshua S Weitz, and Jonathan Dushoff. A practical generation-interval-based approach to inferring the strength of epidemics from their speed. *Epidemics*, 27:12–18, 2019.
- [30] Dimitrios G Patsatzis. On the relation of the covid-19 reproduction number to the explosive timescales: the case of italy. *arXiv preprint arXiv:2101.06101*, 2021.
- [31] Maria Vittoria Barbarossa, Jan Fuhrmann, Jan H Meinke, Stefan Krieg, Hridya Vinod Varma, Noemi Castelletti, and Thomas Lippert. Modeling the spread of covid-19 in germany: Early assessment and possible scenarios. *Plos one*, 15(9):e0238559, 2020.
- [32] M Valorani, F Creta, PP Ciottoli, R Malpica Galassi, DA Goussis, HN Najm, S Paolucci, HG Im, E-A Tingas, DM Manias, et al. Computational singular perturbation method and tangential stretching rate analysis of large scale simulations of reactive flows: Feature tracking, time scale characterization, and cause/effect identification. part 1, basic concepts. In *Data Analysis for Direct Numerical Simulations of Turbulent Combustion*, pages 43–64. Springer, 2020.
- [33] M Valorani, F Creta, PP Ciottoli, R Malpica Galassi, DA Goussis, HN Najm, S Paolucci, HG Im, E-A Tingas, DM Manias, et al. Computational singular perturbation method and tangential stretching rate analysis of large scale simulations of reactive flows: Feature tracking, time scale characterization, and cause/effect identification. part 2,

- analyses of ignition systems, laminar and turbulent flames. In *Data Analysis for Direct Numerical Simulations of Turbulent Combustion*, pages 65–88. Springer, 2020.
- [34] Dimitris M Manias, Shahid Rabbani, Dimitrios C Kyritsis, and Dimitris A Goussis. The effect of fuel additives on the autoignition dynamics of rich methanol/air mixtures. *Fuel*, 323:124275, 2022.
- [35] Athanasios S Fokas, Nikolaos Dikaios, and George A Kastis. Covid-19: predictive mathematical models for the number of deaths in south korea, italy, spain, france, uk, germany, and usa. *medRxiv*, 2020.
- [36] Athanasios S Fokas, Nikolaos Dikaios, and George A Kastis. Predictive mathematical models for the number of individuals infected with covid-19. *medRxiv*, 2020.
- [37] SH Lam and DA Coussis. Conventional asymptotics and computational singular perturbation for simplified kinetics modelling. In *Reduced kinetic mechanisms and asymptotic approximations for methane-air flames*, pages 227–242. Springer, Berlin, Heidelberg, 1991.
- [38] Antonios Zagaris, Hans G Kaper, and Tasso J Kaper. Fast and slow dynamics for the computational singular perturbation method. *Multiscale Modeling & Simulation*, 2(4):613–638, 2004.
- [39] Hans G Kaper, Tasso J Kaper, and Antonios Zagaris. Geometry of the computational singular perturbation method. *Mathematical modelling of natural phenomena*, 10(3):16–30, 2015.
- [40] Efstathios Al Tingas, Dimitrios C Kyritsis, and Dimitris A Goussis. Ignition delay control of dme/air and etoh/air homogeneous autoignition with the use of various additives. *Fuel*, 169:15–24, 2016.
- [41] Dimitris A Goussis and Habib N Najm. Model reduction and physical understanding of slowly oscillating processes: the circadian cycle. *Multiscale Modeling & Simulation*, 5(4):1297–1332, 2006.
- [42] Mauro Valorani, Habib N Najm, and Dimitris A Goussis. Csp analysis of a transient flame-vortex interaction: time scales and manifolds. *Combustion and Flame*, 134(1-2):35–53, 2003.
- [43] Dimitris M Manias, Efstathios-Al Tingas, Yuki Minamoto, and Hong G Im. Topological and chemical characteristics of turbulent flames at mild conditions. *Combustion and Flame*, 208:86–98, 2019.
- [44] Dimitris M Manias, Efstathios-Al Tingas, Francisco E Hernández Pérez, Riccardo Malpica Galassi, Pietro Paolo Ciottoli, Mauro Valorani, and Hong G Im. Investigation of the turbulent flame structure and topology at different karlovitz numbers using the tangential stretching rate index. *Combustion and Flame*, 200:155–167, 2019.
- [45] Dimitris M Manias, Alexandros-Efstathios Tingas, Hong G Im, and Yuki Minamoto. Dynamics analysis of a turbulent methane flame in mild combustion conditions. In *AIAA Scitech 2019 Forum*, page 1731, 2019.
- [46] Dimitris M Manias, Alexandros-Efstathios Tingas, Francisco E Hernandez Perez, Hong G Im, Riccardo Malpica Galassi, Pietro Paolo Ciottoli, and Mauro Valorani. Analysis of hydrogen/air turbulent premixed flames at different karlovitz numbers using computational singular perturbation. In *2018 AIAA Aerospace Sciences Meeting*, page 0364, 2018.
- [47] D.A. Goussis and G Skevis. Nitrogen chemistry controlling steps in methane-air premixed flames. *Computational fluid and solid mechanics*, 1:650–653, 2005.
- [48] Dimitris J Diamantis, Epaminondas Mastorakos, and Dimitris A Goussis. H<sub>2</sub>/air autoignition: the nature and interaction of the developing explosive modes. *Combustion Theory and Modelling*, 19(3):382–433, 2015.
- [49] Dimitris M Manias, Dimitris J Diamantis, and Dimitris A Goussis. Algorithmic identification of the reactions related to the initial development of the time scale that characterizes ch<sub>4</sub>/air autoignition. *Journal of Energy Engineering*, 141(2):C4014015, 2015.
- [50] Dimitris M Manias and Dimitris A Goussis. The initiation of methane/air autoignition: the important chemical components for various initial conditions. In *Journal of Physics: Conference Series*, volume 574, page 012112. IOP Publishing, 2015.
- [51] Dimitris A Goussis. Quasi steady state and partial equilibrium approximations: their relation and their validity. *Combustion Theory and Modelling*, 16:869–926, 2012.